



## Low temperature carburised austenitic stainless steel for metal-on-metal tribological contact



Shaun Maniscalco<sup>a</sup>, Malcolm Caligari Conti<sup>a</sup>, Josianne Cassar<sup>a</sup>, Christian Grima<sup>a</sup>, Andreas Karl<sup>b</sup>, Pierre Schembri Wismayer<sup>c</sup>, Bertram Mallia<sup>a</sup>, Joseph Buhagiar<sup>a,\*</sup>

<sup>a</sup> Department of Metallurgy and Materials Engineering, University of Malta, Msida MSD2080, Malta

<sup>b</sup> Bodycote Specialist Technologies GmbH, Landsberg, Germany

<sup>c</sup> Department of Anatomy, University of Malta, Msida MSD 2080, Malta

### ARTICLE INFO

#### Article history:

Received 23 March 2016

Received in revised form 26 July 2016

Accepted 30 July 2016

Available online 20 September 2016

#### Keywords:

S-phase

Expanded austenite

Carburising

Corrosion

Tribocorrosion

Medical grade austenitic stainless steel

### ABSTRACT

S-phase layers formed on biomedical grade austenitic stainless steels have demonstrated significantly enhanced in-vitro wear and corrosion behaviour. To date, most of these tribo-corrosion studies on S-phase treated alloys were conducted using a polycrystalline alumina or cemented tungsten carbide ball as the counterface material. Testing S-phase against S-phase is both scientifically interesting and technologically important in view of their potential applications for the articulating surfaces of metal-on-metal joint prostheses. In this work, biomedical grade 316LVM discs together with AISI 316 balls were low temperature carburised. In-vitro corrosion-wear testing using an S-phase engineered ball against an S-phase engineered disc was performed. Such testing was also complemented with electrochemical impedance spectroscopy, potentiodynamic and cytotoxicity tests. The results have shown that the carburised 316LVM alloy was found to have good in-vitro cytocompatibility and an augmented corrosion and corrosion-wear resistance when compared with the untreated alloy.

© 2016 Elsevier B.V. All rights reserved.

### 1. Introduction

The favourable corrosion resistance [1–3] and increased surface hardness of carbon S-phase imparted on austenitic stainless steels have already been widely reported in other literature [4]. Studies have also shown that it is possible to produce carbon S-phase layers on medical grade austenitic stainless steel and that there is a possibility for these to be used in orthopaedic applications [1,5,6].

Within the biological environment the material must not illicit an adverse host response by leaching toxic ions by corrosion or corrosion-wear. The interaction among abrasion, rubbing, impact and corrosion can significantly increase total material losses in aqueous environments, thus producing a synergistic effect. The term synergy refers to the enhancement of wear due to corrosion and the change in corrosion rate due to wear. Negative synergism (or antagonism) occurs when the corrosion product during wear provides better protection than the initial surface; an example would be the formation of adherent oxide scale during sliding wear. It is therefore very important to study and in-vitro test newly formed layers holistically in terms of cytotoxicity, corrosion and corrosion-wear response.

The four most common hip joint replacement implants are: polymer-on-metal, ceramic-on-ceramic, polymer-on-ceramic and

metal-on-metal [7]. This means that there is an industrial, medical and scientific interest in the testing of corrosion-wear of metal-on-metal systems. It was proved that carbon S-phase can improve the corrosion-wear response of austenitic stainless steel, however it has always been tested against inert counterfaces. Only one work by Buhagiar et al. [6] has investigated corrosion-wear with both the tribopairs made of the carbon S-phase treated alloy and concluded that there is a huge improvement in wear loss when compared to an untreated-on-untreated system. This improvement was due to a change in wear mechanism from adhesive to mild abrasive wear following S-phase engineering. The combined wear of S-phase against S-phase was close to that of the cobalt-based tribopair (material of choice in metal-on-metal hip joint replacement) under reciprocating sliding wear conditions in Ringer's solution. However the work by Buhagiar et al. [6] does not make use of electrochemical techniques in order to calculate the percentage of material loss due to synergy [8].

Independent studies have confirmed that a carbon rich S-phase results in an improvement of the hardness [4] and wear [9] and corrosion-wear [6,10] system response without any detriment to the corrosion resistance [1–3,11–13]. However no work has been done to evaluate the S-phase cytocompatibility except for two studies on low temperature carburising of: austenitic stainless steel [5]; and cobalt-chromium-molybdenum [12]. Both studies [5,12] have confirmed that carbon S-phase layers formed on these two materials did not reduce the biocompatibility of their respective untreated alloys.

\* Corresponding author.

E-mail address: [joseph.p.buhagiar@um.edu.mt](mailto:joseph.p.buhagiar@um.edu.mt) (J. Buhagiar).

This work presents a holistic view in terms of material characterisation of carbon S-phase formed on austenitic stainless steel in terms of its suitability in the multidisciplinary field of biomedical orthopaedic implants. It characterises the surface of a carburised stainless steel and then analyses its corrosion, corrosion-wear and cytocompatible response in an in-vitro environment.

## 2. Material and methods

### 2.1. Test materials

The materials used in this study consisted of AISI 316LVM stainless steel for surgical implants as per ASTM F138 supplied by L. Klein SA (Switzerland) as rolled round bars of diameter 25.4 mm and AISI 316L supplied by Spheric Trafalgar Ltd. (UK) in spherical form having a diameter of 12.7 mm. The chemical composition of the material in either form is known through a material certificate and is represented in Table 1.

The as-supplied AISI 316LVM bar material was turned on a lathe to two different diameters 25.00 mm and 9.52 mm and cut into coupons of 6 mm and 2 mm thickness respectively. Some of the spheres, to be used for characterisation, had two caps on opposite sides ground off. The flat surfaces of the coupon material were wet-ground using silicon carbide paper from P120 to P1200 grit. The ground surfaces were polished using 6  $\mu\text{m}$  and 3  $\mu\text{m}$  diamond pastes (MetPrep UK) in conjunction with their respective polishing cloths. An ultrasonic bath in acetone and successive drying in hot air was employed prior to every polishing stage, as well as at the end to remove any surface contaminants.

The polished 25.00 mm and 9.52 mm diameter disc coupons, the as-received spheres and the capped off spheres were subjected to a low temperature carburising diffusion-based surface treatment by Bodycote Specialist Technologies GmbH (Landsberg, Germany). During this diffusion surface treatment, the samples were exposed to temperatures below 500 °C and high carbon potentials for several days to obtain a precipitate free S-phase layer.

### 2.2. Positive control materials

As a control material for the metal-on-metal corrosion-wear tests a Cobalt-Chromium-Molybdenum (CoCrMo) alloy was selected. The 25 mm diameter control disc coupons were made from a wrought unannealed CoCrMo surgical implants alloy (Biodur® CCM) as per ASTM F1537, supplied by L. Klein SA (Switzerland). The 12.7 mm diameter control balls were made from sintered CoCrMo Stellite® 21, supplied by Kennametal (Italy). The chemical composition of the material in either form is known through a material certificate and is represented in Table 2, mirroring respective material certification.

As a positive control for the cytocompatibility experiments Thermanox™ Coverslips (Thermo Scientific™ Nunc™, USA) were used. These are polyester film strips with very low oxygen content having a hydrophilic surface to increase cell adherence. These films were laser cut into discs 9.52 mm in diameter.

### 2.3. Preliminary material characterisation

The material characterisation mentioned in this section was performed on low temperature carburised 25 mm diameter austenitic

**Table 2**  
Compositions of the CoCrMo (control) materials used, wt%.

		C	Si	Mn	Fe	W	Mo	Ni	Cr	Co
Disc	ASTM F1537	0.05	0.62	0.80	0.20	–	5.46	0.07	27.64	Bal.
Sphere	Stellite® 21	0.23	1.50	0.45	0.80	0.13	5.50	2.80	26.80	Bal.

stainless steel coupons and capped off austenitic stainless steel spheres which were cleaned with acetone in an ultrasonic bath.

Standard procedures were followed to prepare metallographic specimens to be examined under a Nikon OPTIPHOT-100 optical microscope. In order to image the S-phase layer created in the carburised 25 mm diameter disc coupon, sectioning normal to the flat surface was performed. This was followed by mounting in Struers Polyfast mounting resin. On the other hand the capped off carburised sphere coupon was mounted on a Struers Taper section with an angle of 10° and then cold mounted in resin. The two mounted specimens were then ground to a P1200 grit using silicon carbide abrasive paper. Samples were then initially polished using 6  $\mu\text{m}$  and 3  $\mu\text{m}$  polycrystalline diamond paste (MetPrep UK) followed by a final polish using chemically active suspended aluminium oxide abrasive (Struers OP-AA). The surfaces were then chemically etched in a solution containing 50 ml of HCl (39% conc.), 25 ml of HNO<sub>3</sub> (69% conc.) and 25 ml of distilled water.

Chemical characterisation of carburised 25 mm austenitic stainless steel disc coupon specimens was accomplished via a LECO GDS-750 QDP Glow Discharge Optical Emission Spectroscopy (GDOES) machine. Calibration was first conducted such that the equipment was set up for all the alloying elements present in the stainless steel with particular attention to carbon. This type of analysis consented for the measurement of the carbon content at increasing depth from the surface of the carburised coupons.

The phase constituents in the untreated and carburised austenitic stainless steel disc and capped off sphere coupons were studied by means of Glancing-Angle X-Ray Diffraction (GAXRD) using a Rigaku Ultima IV diffractometer (CuK $\alpha$  radiation,  $\lambda = 0.154 \text{ nm}$ ) operated in Grazing Incidence Asymmetric Bragg (GIAB) geometry. The incident angle used was set at 3° with a sampling width of 0.05°, and a scan speed of 0.8 s/step in the 30° to 100° 2 $\theta$  range. The tube acceleration voltage applied was 40 kV while the current was 30 mA.

Microhardness indentations were carried out using a Mitutoyo MVK-H2 with a Vickers hardness indenter. Ten repeated indentations were made on the surface at a load of 100 gf and care was taken to ensure that each indent was at least 5 diameters away from the previous indent.

In order to obtain a hardness versus depth profile of the carbon diffusion layer formed, the austenitic stainless steel disc and capped off sphere were cold mounted on taper section angles (Struers). This inclined the sample by 10° and therefore provided more space for indentations since the layer's depth was magnified by an order of 5. The mounted samples were metallographically polished and nano-indentation was carried out on the magnified treated layer using a Micromaterials NanoTest (UK) equipped with a diamond Berkovich indenter at a load of 100 mN. Each indent was carried out by using computer control to start at a load of 0.1 mN and gradually increasing by a rate of 2 mN s<sup>-1</sup> until the pre-set load was reached. The load then ramped down at the same rate of 2 mN s<sup>-1</sup>. A set of 25 indents was performed, with the first indent effected at the surface of the sample layer. The location of indents was set such that every subsequent indent

**Table 1**  
Compositions of the stainless steel materials used, wt%.

		C	Si	Mn	P	S	N	Cu	Mo	Ni	Cr	Fe
Disc	316LVM	0.011	0.25	1.69	0.016	0.003	0.088	0.03	2.78	14.56	17.33	Bal.
Sphere	316L	0.08*	1.0*	2.0*	0.045*	0.03*	–	–	2–3	10–14	16–18	Bal.

\* Represents maximum value.

approached the substrate while avoiding the deformation zone introduced by the previous indent. The process was repeated so as to obtain 3 sets of 25 indents. The indents were examined under a Nikon Optiphot-100 optical microscope to determine their distance from the surface of the sample.

Roughness measurements were carried out using an AEP nanomap 500LS (AEP technology, USA) contact profilometer. The untreated 316LVM, carburised 316LVM and Thermanox® samples were placed beneath the stylus and a roughness measurement was taken using a profilometer with a vertical range of 5  $\mu\text{m}$ , a load of 10 mg and a length of 2000  $\mu\text{m}$ . The roughness measurement was repeated on five different samples for each of the carburised, untreated and Thermanox® samples.

Contact angle measurements were performed following ASTM D7334 - 13 - *Standard Practice for Surface Wettability of Coatings, Substrates and Pigments by Advancing Contact Angle Measurement*. The untreated and carburised 316LVM samples were cleaned thoroughly using ethanol, followed by acetone, followed by deionised water. 30  $\mu\text{l}$  of deionised water was then pipetted using a P200 pipette (Gilson, USA) onto each sample. The image was then captured using a camera (Veho, Discovery VMS-004, Worldwide) connected to a computer. Sessile drop analysis was then performed using Image J (Open Source). The testing was repeated on 5 different samples for both the carburised and untreated 316LVM alloy as well as the Thermanox® cover slips.

#### 2.4. Cytotoxicity testing

hFOB 1.19 (American Type Culture Collection™) human foetal osteoblast cells were cultured in Dulbecco's Modified Eagle's Medium with F12 (Life Technologies (Gibco) International), with 10% Fetal Bovine Serum (Life Technologies (Gibco) International) and 1% Penicillin/Streptomycin (Sigma Aldrich™).

Cultures were incubated in 5% (v/v) carbon dioxide at 37 °C. Cells were harvested using a 1% Trypsin solution (Life Technologies (Gibco) International) and a suspension containing 30,000 cells  $\text{ml}^{-1}$  was used for the viability assay.

The metallic discs (9.52 mm diameter; 2 mm thickness) and control polyester samples (9.52 mm Thermanox™ coverslips) were placed in the (15.6 mm diameter) wells of 24-well plates (Orange Scientific, Belgium). Four replicate samples of each material type were used for each time point with an additional sample for SEM. A cell suspension containing 30,000 cells/ml was prepared and 1 ml of this was added per well. Cultures were incubated for 1, 2, 3 and 4 days.

Viable cell numbers were compared by an MTT test, which is based on the reduction of tetrazolium salt to formazan. This reduction is affected by both changes in cell number and cell metabolism. 100  $\mu\text{l}$  of MTT (3-(4,5-dimethylthiazol-2-yl)-2,5-diphenyltetrazolium bromide); 5 mg/ml; (Alfa Aesar, Germany) solution in PBS were added to the wells containing samples to be assayed. The plate was then placed on a plate shaker and shaken at 300 rpm for 5 min and then incubated for 4 h in order for the cells to metabolize the MTT.

Each metallic disc and Thermanox coverslip control was then transferred into a new 24-well plate (in order to assay only the cells growing solely atop the samples and not on the edges of the polystyrene well) and 400  $\mu\text{l}$  of dimethylsulphoxide (Sigma™) was added. The plate was then placed on a plate shaker and shaken at 300 rpm for 5 min to solubilise the formazan. 100  $\mu\text{l}$  of the resulting solution of each well was then pipetted to corresponding wells in a 96 well plate and transferred to a spectrophotometer where the absorbance was read at  $\lambda = 570$  nm with a reference wavelength of  $\lambda = 650$  nm. The whole procedure was repeated twice in order to show experiment repeatability.

Absorbance readings were converted to cell number by reference to a calibration graph. The calibration graph included MTT absorbance readings for cell seeding densities ranging from 5000 cells/ml to 50,000 cells/ml and from 60,000 cells/ml to 100,000 cells/ml in increments of 5000 cells/ml and 10,000 cells/ml respectively.

#### 2.5. Electrochemical testing

In order to assess whether low temperature carburising of austenitic stainless steel would be a viable treatment within the biomedical scenario; corrosion (potentiodynamic and EIS) and corrosion-wear screening were conducted in in-vitro conditions.

All electrochemical tests were conducted using a 3-electrode setup, consisting of a reference Saturated Calomel Electrode (SCE) (Gamry Instruments) inside a Luggin Capillary, a platinum counter electrode and the working electrode (untreated and carburised 25 mm diameter disc coupons).

The electrolyte used in this research is Ringer's solution, supplied by Lab M (UK) in tablet form. The solution's chemical composition is 9  $\text{g L}^{-1}$  NaCl; 0.42  $\text{g L}^{-1}$  KCl; 0.48  $\text{g L}^{-1}$   $\text{CaCl}_2$ ; 0.2  $\text{g L}^{-1}$   $\text{NaHCO}_3$ . Having a pH of 7.4, Ringer's solution provides a good representation of bodily fluids. All tests were conducted at  $37 \pm 1$  °C and each test was performed at least three times to ensure repeatability of results.

##### 2.5.1. Potentiodynamic testing

Electrochemical tests were performed using a Gamry Interface 1000™ potentiostat/galvanostat/ZRA using a 3-electrode setup and with a 1.8  $\text{cm}^2$  of the test sample being exposed to 300 ml of Ringer's solution.

The procedure included an initial OCP scan in which the Ringer's solution was degassed by supplying nitrogen into it for 1 h. A second OCP scan followed exactly afterwards. Like the previous one, this scan lasted 1 h, however no nitrogen was supplied during this interval. Cyclic polarisation sweeps were then scanned at a rate of 0.17 mV/s between the following ranges: – 100 mV versus OCP and 1000 mV versus reference. The polarisation scan was reversed at a scan rate of 0.17 mV/s when either an apex potential of 1000 mV versus reference or an apex current of 0.5  $\text{mA/cm}^2$  was reached. The test was terminated at potential of 0 mV versus the OCP.

##### 2.5.2. Electrochemical impedance spectroscopy testing

Electrochemical impedance spectroscopy measurements involved the use of a three-electrode corrosion test cell, using a Gamry Instruments Reference 600™ potentiostat, which is also equipped to read EIS measurements (frequency response analyser). The sequence of the procedure together with the relevant parameters was programmed through the Gamry Framework™ software. The working electrode was pressed between a copper backing disc and an o-ring, such that a surface area of 1.8  $\text{cm}^2$  was exposed to the electrolyte.

Prior to inserting the samples into the electrochemical cell, a 45-minute cleaning procedure was applied before each test in order to ensure uniformity in the surface conditions of the samples. The first step was to clean the sample's surface with sodium laureth sulphate and water, followed by 15 min of ultrasonic cleaning in isopropyl alcohol. The sample was then polished with 3  $\mu\text{m}$  diamond paste; the untreated samples were polished for approximately 5 min while the treated samples were polished for 2 s in order not to remove the surface treatment. The polishing was followed by 15 min of ultrasonic cleaning in isopropyl alcohol and drying with hot air. After 45 min from the start of the cleaning procedure, the sample was inserted into the cell. This procedure was done such that each and every test started off with the same surface conditions.

Before the impedance spectra were measured, the 300 ml of Ringer's solution was de-gassed with nitrogen for 1 h, and then the open circuit potential for the combination was monitored for another hour. The EIS measurement was then carried out with the interface impedance measured with respect to the last OCP recorded before EIS commencement. The range of frequencies for the impedance spectra were varied from 10,000 Hz to 0.004 Hz with ten points per decade, and using a sinusoidal signal of 10 mV (RMS). The results from these tests were represented in Bode and Nyquist plots. Equivalent electrical circuits (EECs) were

modelled through Echem Analyst™ software by means of the Simplex mathematical algorithm.

### 2.5.3. Tribocorrosion testing

A tribocorrosion tester satisfying the requirements of ASTM G133 - 'Standard Test Method for Linearly Reciprocating Ball-on-Flat Sliding Wear' was used. All tribocorrosion electrochemical measurements were performed using a Gamry Interface 1000™ potentiostat/galvanostat/ZRA using a 3-electrode setup. This consisted of a reference Saturated Calomel Electrode (SCE) (Gamry Instruments), a platinum counter electrode and the working electrode (WE). The WE had the following areas exposed to 300 ml of Ringer's solution: 3.7 cm<sup>2</sup> of the flat test sample area and approximately 1.3 cm<sup>2</sup> of the ball counterface. The tribocorrosion tests were performed under two potential conditions: cathodic (−700 mV vs. SCE) and open circuit potential.

Tribocorrosion tests were performed using sphere-on-flat tribopair configurations on untreated-against-untreated stainless steel, carburised-against-carburised stainless steel and CoCrMo-against-CoCrMo (control). The CoCrMo tribopair was used as a benchmark because this is the material currently being used in metal-on-metal hip joint prosthesis. The wear component in this tribocorrosion system was initiated by linearly reciprocating the coupon sample against the stationary 12.7 mm sphere under a normal load of 4.9 N, a stroke length of 7.6 mm and an oscillation frequency of 1 Hz.

The initial Hertzian contact pressures for the tribocorrosion system were calculated from the static setup. The values obtained for the stainless tribopair and CoCrMo tribopair were of 650 MPa and 727 MPa respectively. These high Hertzian stresses are not representative of the typical joint replacement environment, however the 4.9 N load was necessary in order to be able to have a measurable wear on the carburised and control specimens within a reasonable testing period of 2 h. Post-wear examination of the cross-sections of the wear tracks was conducted on all specimens and no gross plastic deformation could be detected within the microstructure close to the tested surface.

The protocol followed for testing involved pouring 300 ml of Ringer's solution into the testing cell. In the cathodic test experiments a voltage of −700 mV vs. SCE was applied and the current monitored. In the case of the OCP tribological tests, no external potential was applied and the OCP was recorded during the test.

The ball was then loaded onto the flat disc sample in the solution and measurements for the voltage (OCP test) or current (cathodic test) were taken for 600 s. At the 600 s mark, sliding was initiated and the voltage (OCP test) or current (cathodic test) and friction (for all tests) were measured. After 2 h of sliding, the reciprocating motion was stopped and the voltage (for the OCP test) and current (for the cathodic test) were measured for a further 600 s.

Following tribocorrosion, characterisation of the wear scar morphologies on the tribopair specimens was executed with a Carl Zeiss MERLIN series SEM equipped with a high resolution GEMINI II column and an Apollo EDAX EDS detector for chemical analysis.

The SEM image of the ball was also used to obtain the diameter of the circular wear scar. By applying Pythagoras theorem and using the values of the original diameter of the spherical ball ( $a = 6.35$  mm) and the measured radius of the wear scar; the perpendicular height ( $h$ ) of the spherical cap was calculated. The volume of material lost from the ball was then calculated using Eq. (1).

$$V = \frac{\pi h^2 (3a - h)}{3} \quad (1)$$

The profile of the wear track was obtained using the Ambios Xp-200 Stylus surface profilometer. This profile was used to obtain the cross sectional area of each wear scar at 3 separate locations, avoiding measurements close to the wear scar edge. The average area obtained was then multiplied by the length (7.6 mm) of the wear track to obtain the wear volume lost on the disc sample.

Utilising the wear volume data (ball and disc) the total amount of wear ( $T$ ) was obtained from the OCP test and the independent mechanical wear ( $W_o$ ) was obtained from the cathodic test. These values were then substituted in Eq. (2), where the independent corrosion ( $C_o$ ) component was assumed to be zero due to the fact that the materials used in this study are passive. Therefore, the synergy ( $S$ ) of the system was calculated by the subtraction of  $W_o$  from  $T$ .

$$T = W_o + C_o + S \quad (2)$$

## 3. Results

### 3.1. Treatment characterisation

The carburising treatment yielded a diffusion layer of circa 40 μm with a surface carbon interstitial content of 21 at% at the immediate surface. The stainless steel ball and disc used in this work are single phased. After carburising the FCC  $\gamma$ -phase XRD peaks got broader and shifted to low angles. Some very minor cementite ( $Fe_3C$ ) and Hägg Carbides ( $Fe_5C_2$ ) precipitates were present. The layer's hardness shown in Table 3 shows an increase by  $347 \pm 1\%$  for the disc and  $189 \pm 2\%$  for the ball after treatment. Fig. 1 shows the hardness profile of the layer which corroborates well with the 40 μm layer thickness and microhardness data in Table 3.

Based on the chemical, phase analysis and hardness (Table 3) results it can be deduced that a precipitate-free metastable supersaturated solid solution layer of carbon (S-phase or Expanded Austenite) was created on both ball and disc austenitic stainless steel. It can be confirmed that the disc and ball responded in a very similar fashion to the carburising treatments as only very minor differences were noted.

### 3.2. Biological response

Table 3 provides the surface characteristics related to the materials used in the cytocompatibility experiments. The results in Fig. 2 show that the human foetal osteoblast cell line grows well on both the untreated and the carburised 316LVM samples. Both samples reach approximately the same levels of growth after four days. This resembles the results of the Thermanox® positive control samples where the level of growth is observed to increase gradually to approximately 180% of the initial value of cell density. The rapid growth of the human foetal osteoblasts on the untreated, carburised and Thermanox® samples was also visualised by microscopy techniques (not presented in this paper). Cells were observed to grow from a low confluency  $\approx 30\%$  on day 1 to a quasi-confluent monolayer on top of all the samples tested by day 4. This points to the overall cytocompatibility of the carburised stainless steel.

### 3.3. Corrosion response

The carburising treatment improved the localised corrosion resistance of the untreated material. The untreated alloy suffered from metastable pitting which changed into stable pit formation at a potential of  $550 \pm 173$  mV versus SCE (refer to Table 3). Moreover, cyclic polarisation scans on untreated samples have revealed a repassivation potential ( $E_{prot}$ ) in the region of 100 and 200 mV versus SCE. On the other hand, the carburised alloy did not suffer from any localised corrosion.

Fig. 3 superimposes the Nyquist and Bode plots attained when testing untreated and carburised austenitic stainless steel. Note that the EIS plots depicted in this section correspond to one test which is the best representative of all tests carried out at that particular condition. Furthermore, EEC parameter errors correspond to the chosen (best representative) plot only, and relate the discrepancy between the actual EIS plot (result) and the EEC fit (model).

**Table 3**

Contact angle, roughness, hardness and corrosion results.

	$R_a$ (nm)	Contact angle (°)	Hardness disc HV100	Hardness sphere HV100	OCP mV	$E_{pit}$ mV
Untreated	13.0 ± 1.3	43 ± 3	262 ± 5	367 ± 13	-180 ± 30	550 ± 173
Carburised	163.3 ± 10.9	30 ± 2	1170 ± 20	1058 ± 30	-200 ± 20	>1000
Thermanox®	12.3 ± 0.6	69 ± 1	-	-	-	-

The EEC used to model the metal/electrolyte interface of this system is shown in Fig. 3 (inset); the model is made up of two resistor-capacitor combinations in series, together with the solution resistance  $R_s$  (which reflects the ohmic drop). The untreated and treated surfaces were modelled by the same EEC since it was assumed that the components of the interface of both surfaces would be the same. The discrepancy between the two surfaces would hence be in the circuit parameter values rather than the model itself. Using the same EEC is also required for comparison purposes.  $R_1$  and  $CPE_1$  are representative of the charge transfer processes which occur at the electrical double layer (EDL), this being the outer layer of the combination. The EDL is characterised by a capacitor because it is known that this electrical element represents the physical separation of oppositely charged planes; charge separation, between metal ions and electrons occurs at an EDL and hence the capacitor represents this characteristic. The resistance, on the other hand, is representative of the layer's inherent characteristic of resisting the transfer of excess electrons to electrochemically active species [14]. Hence  $R_1$  is the charge transfer resistance and  $CPE_1$  is the capacitance associated with the EDL; this parallel combination constitutes one time constant. The second parallel combination is connected to the working electrode and it represents the passive layer, this providing the second time constant.  $R_2$  represents the resistance of the oxide layer while  $CPE_2$  represents its capacitance. The motion of charge species and vacancies through the passive layer at the lower frequencies is hence characterised by this latter parallel combination [15,16]. The summation of charge transfer resistance ( $R_1$ ) and the oxide layer resistance ( $R_2$ ) represents the polarisation resistance [17].

The circuit makes use of a constant phase element rather than capacitance. This element is necessary since the assumption of an electrode surface being uniformly active is not suitable. Variation in current, potential and reactivity occurring along the electrode surface leads to time constant dispersion, as well as distributed properties of oxide layers [18]. Therefore, when the metal/electrolyte interface's behaviour

deviates from what is expected from an ideal response of a single electrochemical reaction, a CPE is used for modelling impedance spectra. The time constant dispersion was associated with capacitance distribution, or variation of capacitance resulting from frequency variation [19]. Jorcin et al. [19] suggests other factors leading to the distribution of capacitance, hence CPE behaviour (other than distributions of surface reactivity): surface heterogeneity and roughness, with the former being more significant than the latter, fractal geometry, electrode porosity and electrode geometry leading to current and potential distributions mentioned previously. Microscopic features such as grain boundaries, dislocations and impurities also contribute to CPE behaviour [16]. There are various expressions representing the impedance of a CPE, but the most commonly used is shown in Eq. (3) [19,20]:

$$Z = \frac{1}{Q(i\omega)^\alpha} \quad (3)$$

$Q$  is the CPE constant and  $\alpha$  is the CPE exponent; the latter parameter varies according to the behaviour of the layer. When  $\alpha = 1$ , the CPE represents a capacitor,  $\alpha = 0.5$  represents Warburg impedance,  $\alpha = 0$  represents a resistor and  $\alpha = -1$  an inductor [21,22]. Therefore, the unit of parameter  $Q$  depends on  $\alpha$ . Orazem et al. [18] tries to achieve conformity by stating that when  $\alpha = 1$ ,  $Q$  has the units of capacitance,  $F/cm^2$ , and the CPE should be considered as a capacitor. When  $\alpha \neq 1$ , surface heterogeneity or the continuous distribution of time constants for

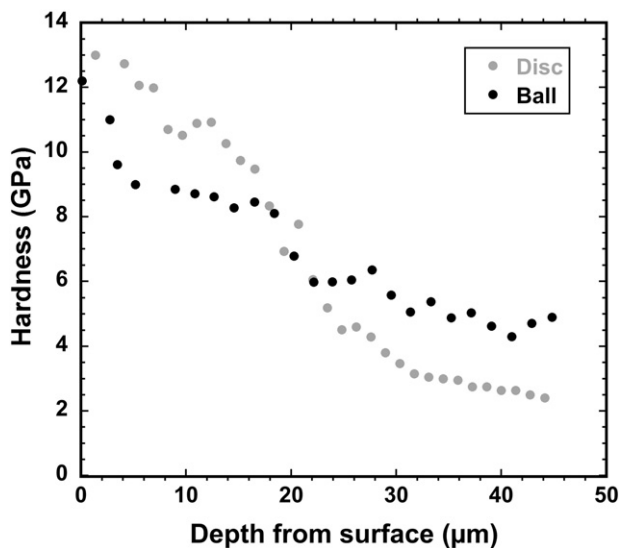


**Fig. 1.** Hardness depth profile of a carburised 316L ball and 316LVM disc specimen indented in the cross section using a Berkovich indenter at a load of 100 mN.

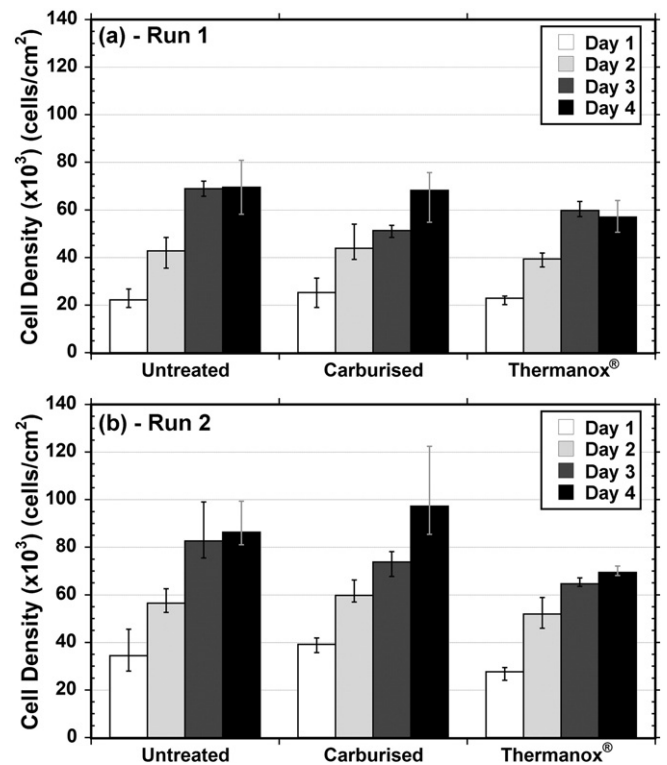


**Fig. 2.** MTT results for the human foetal osteoblast cell line (hFOB1.19) on untreated 316LVM, carburised 316LVM and Thermanox® for the (a) first and (b) second experimental run. Error bars reflect the range of values for  $n = 4$ .

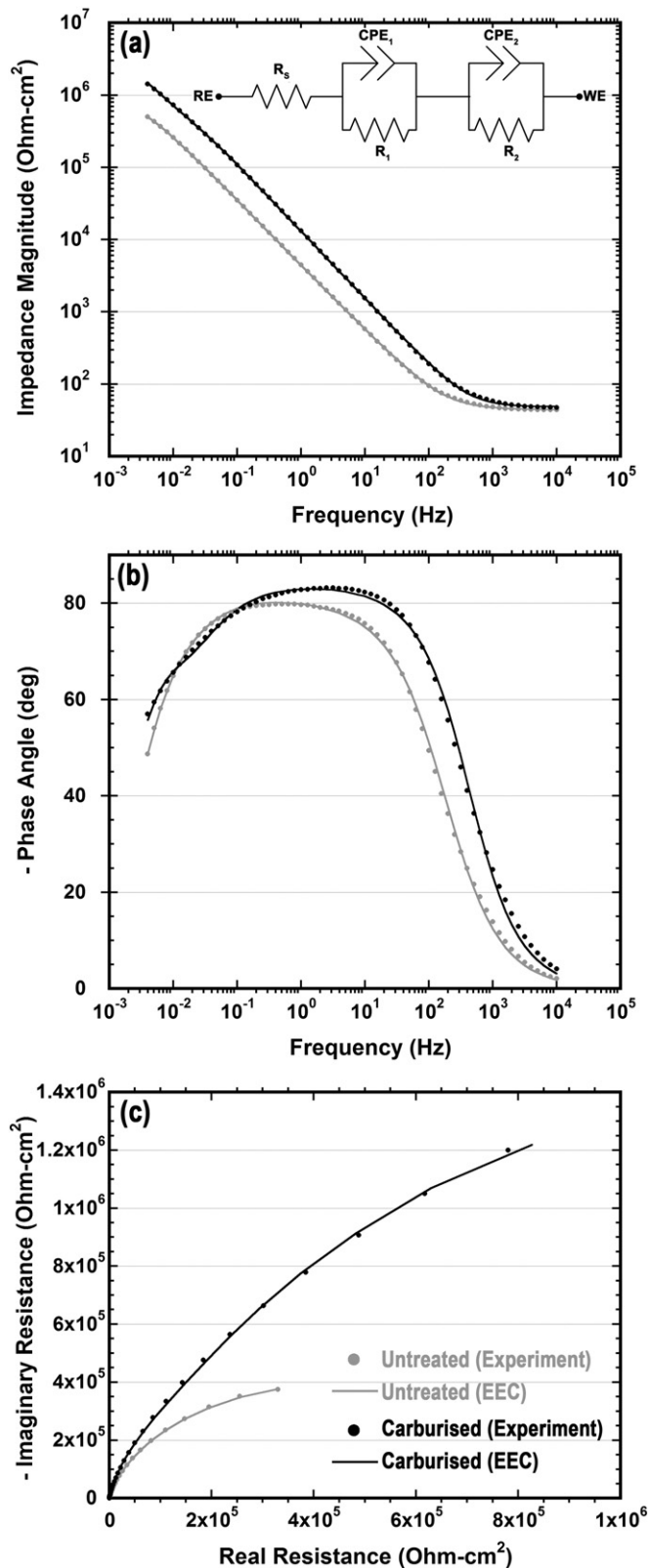


Fig. 3. Bode-magnitude (a), Bode-phase (b) and Nyquist (c) plots attained during EIS testing at the equilibrium potential of 316LVM alloy, together with their EEC model fit.

charge transfer reactions modify the ideal-capacitor behaviour, this being represented by CPE, and  $Q$  has units of  $s^\alpha/\Omega\text{cm}^2$  (or  $S\text{ s}^\alpha/\text{cm}^2$ ).

Table 4 illustrates the circuit parameters resulting after modelling the metal/electrolyte response with the EEC shown in Fig. 3 (inset).

The goodness of fit value represents the Chi-squared value divided by the total number of points in the spectra [23].

### 3.4. Metal-on-metal corrosion-wear response

#### 3.4.1. Cathodic potential

The current and friction versus time results following repeated potentiostatic tests at  $-700\text{ mV}$  (vs SCE) on the untreated and carburised stainless steel metal-on-metal combinations are shown in Fig. 4. On the onset of sliding, the cathodic current increased in magnitude (Fig. 4a) for both the untreated and carburised material with the latter experiencing somewhat higher cathodic currents. The most prominent difference between untreated and carburised tribopair plot is the high amplitude oscillations in current experienced by the carburised tribopair after few minutes of sliding when compared to the untreated. The coefficient of friction (CoF) plot (Fig. 4b) exhibits identical behaviour between untreated and carburised tribopairs during the initial running-in period. The CoF of the untreated tribopair stabilised at a value of circa 0.55 while that of the carburised tribopair stabilised after a longer sliding period at a value of circa 0.75.

The wear scar morphologies of the ball and disc for tests under cathodic potential conditions are shown in Fig. 5. A marked difference can be observed between the resultant wear track morphologies on untreated and carburised stainless steel as shown in Fig. 5a and c. The untreated disc wear scar (Fig. 5a) has a roughened surface characterised by abrasion marks in the direction of sliding and local plastic deformation and material detachment. The carburised disc wear scar resulted in a smooth surface with no evidence of abrasion grooves containing small dispersed patches of smeared fine wear debris typical of polishing wear.

The ball wear scar in Fig. 5 (b) and (d) are circular and contain abrasion marks aligned with the direction of sliding. The carburised ball resulted in a smaller wear scar size. The untreated wear scar has wear debris concentrated primarily at the perimeter of the scar and evidence of smeared material.

#### 3.4.2. Open circuit potential

The OCP and dynamic friction versus time following repeated tests under open circuit potential conditions on the untreated and carburised stainless steel metal-on-metal combinations are shown in Fig. 6. Upon initiation of sliding the potentials instantaneously experience a cathodic drop which was recovered upon termination of sliding. There are two notable differences between the untreated and carburised systems: (1) The untreated stainless steel tribopair plot has a constantly lower OCP value than the carburised tribopair plot both at rest and also during sliding; and (2) The untreated tribopair plot displays large OCP fluctuations during sliding in contrast to the carburised counterpart. The friction coefficient of the carburised tribopair stabilised at a higher value to that of the untreated. The same trend was observed for tests under cathodic protection. In this case, however the CoF trace for the untreated displayed frequent fluctuations between 0.3 and 0.5.

The wear scar morphology of the ball and disc for the open circuit potential is shown in Fig. 7. A marked different morphology between the untreated and carburised stainless steel wear tracks on the discs resulted as shown in Fig. 7a and c. The untreated disc wear track at OCP (Fig. 7a) displayed a roughened surface with evidence of abrasion marks in the direction of sliding and extensive localised plastic deformation and material detachment. The carburised disc wear scar (Fig. 7c) contained small abrasion marked aligned in the direction of sliding and no evidence of local plastic shearing. The scar on the carburised ball following testing under OCP (Fig. 7 d) is largely featureless and circular in shape. The scar on the untreated ball (Fig 7b) had an elliptical shape with a roughened morphology and material transfer and detachment.

**Table 4**

EEC parameters obtained after modelling EIS results with circuit consisting of two RC combinations in series.

	$R_s$ ( $\Omega$ cm <sup>2</sup> )	$R_1$ (k $\Omega$ cm <sup>2</sup> )	$R_2$ (k $\Omega$ cm <sup>2</sup> )	$Q_1$ ( $\mu$ S s <sup>0.5</sup> /cm <sup>2</sup> )	$\alpha_1$	$Q_2$ ( $\mu$ S s <sup>0.5</sup> /cm <sup>2</sup> )	$\alpha_2$	Goodness of fit ( $10^{-6}$ )
Untreated	44.36	126.70	708.90	89.44	0.82	78.95	0.97	325.0
Carburised	48.57	283.30	2845.00	27.04	0.88	27.19	1.00	689.1

### 3.4.3. Wear loss

Fig. 8 shows the material volumetric loss on the disc (Fig. 8a) and the ball (Fig. 8b). Data for a metal-on-metal CoCrMo tribopair was also included so that it could be used as a benchmark owing to the fact that this system is the one used in current metal-on-metal systems.

Analysing Fig. 8 it is clear that the material lost for all materials tested under OCP conditions is always higher compared to those tested under cathodic potential conditions. The material lost by the ball is always relatively smaller to the material lost by the disc. The percentage wear loss reduction of the system (disc and ball) following carburising, calculated from the mean total volumetric losses, is 70% and 80% for the cathodic and open circuit potentials respectively compared to the respective untreated discs. This improvement allows the carburised material to approach the CoCrMo tribopair which, calculated from the mean total volumetric losses, has a 70% wear loss reduction when compared to the carburised material.

## 4. Discussion

### 4.1. Cytocompatibility

The results of the in-vitro cytocompatibility tests (Fig. 2) reported in this work have demonstrated that neither carburised nor untreated

samples showed any adverse effect on the proliferation of the human foetal osteoblast cells used. The change in hydrophilicity, roughness (Table 3) and surface chemistry of the stainless steel post-carburising had little, if any, effect on the performance of the cells grown on the specimens. In addition, the corrosion results (Fig. 3) show that carburising had a profound effect on the EDL and the passive film of the material. However, this also seems to have no affect on the cells, mainly due to the fact that the corrosion resistance of the untreated material is already effective enough to stop the leaching of potential toxic ions to the cell culture medium over the period of days tested.

### 4.2. Corrosion

The Nyquist plots within Fig. 3 give an immediate indication of the metal/electrolyte's overall impedance; the graphs show that surface treatment enhanced the interface's impedance, thus improving its protectiveness against corrosion. From the resulting parameter values in Table 4, it is evident that both the passive layer resistance and EDL's charge transfer resistance increased considerably after carburising. The passive layer resistance (represented by  $R_2$ ) of the investigated austenitic stainless steel increased from 708.90 k $\Omega$  cm<sup>2</sup> before carburising to 2845.00 k $\Omega$  cm<sup>2</sup> after carburising.

Stability and distribution of capacitance within the passive layer improved as well since the exponent of CPE<sub>2</sub>, denoted as  $\alpha_2$ , became unity, therefore indicating that the passive layer was now a perfect capacitor. This implies that the distribution of voltage, current and reactions along the passive layer was reduced and hence the variation of time constants along the layer was, consequentially, reduced if not eliminated. In turn, this means that the S-phase provided a good and stable bed for the passive layer, and although surface roughness (Table 3) increased after the treatment, the layer still acted as a perfect capacitor. Hence one may conclude that the distribution of capacitance or time constant is not directly related to the surface roughness.

The CPE constant associated with the passive film,  $Q_2$ , is converted to capacitance through Eq. (4) [24–27]:

$$Q_2 = R_2^{\alpha_2 - 1} C^{\alpha_2} \quad (4)$$

This conversion is required since the parameter  $Q_2$  is not capacitance, even when the CPE exponent is close to unity [28]. This was done to associate a change in capacitance with possible modifications in the layer under investigation. Capacitance is directly related to the dielectric constant and inversely related to layer thickness through the relationship in Eq. (5):

$$C = \frac{\epsilon \epsilon_0 A}{d} \quad (5)$$

It is important to note that the conversion ( $Q \rightarrow C$ ) can only lead to assumptions on the characteristics (thickness, composition) of the layer since changes in the dielectric constant, particularly related to composition (layer constituents, hydration) and morphology, are unknown [25,29–31]. In addition, Wallinder et al. [32] point out that the effective area of the layer (hence capacitor) differs from the geometric area because of roughness.

The capacitance of the passive film associated with untreated 316LVM was calculated to be 89.42  $\mu$ F/cm<sup>2</sup>, while that associated with the carburised metal was 27.19  $\mu$ F/cm<sup>2</sup>. Therefore, there is the possibility that the carburised metal's passive film is thicker than the untreated

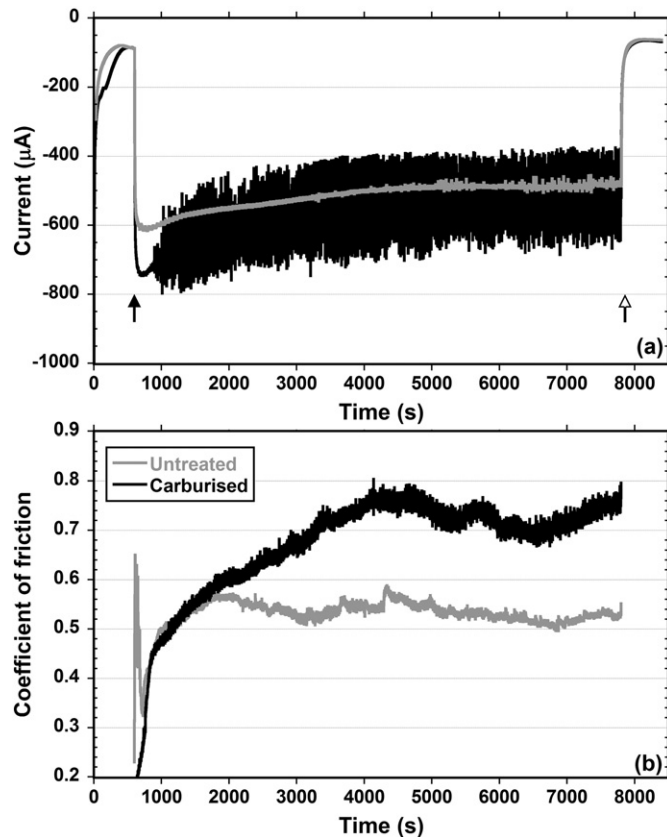


**Fig. 4.** Cathodic potential ( $-700$  mV vs. SCE) plots for untreated-on-untreated and carburised-on-carburised stainless steel tribopairs during reciprocating sliding in Ringer's solution of (a) current and (b) coefficient of friction, as a function of time. Black arrow indicates onset of sliding and white arrow indicates termination of sliding.

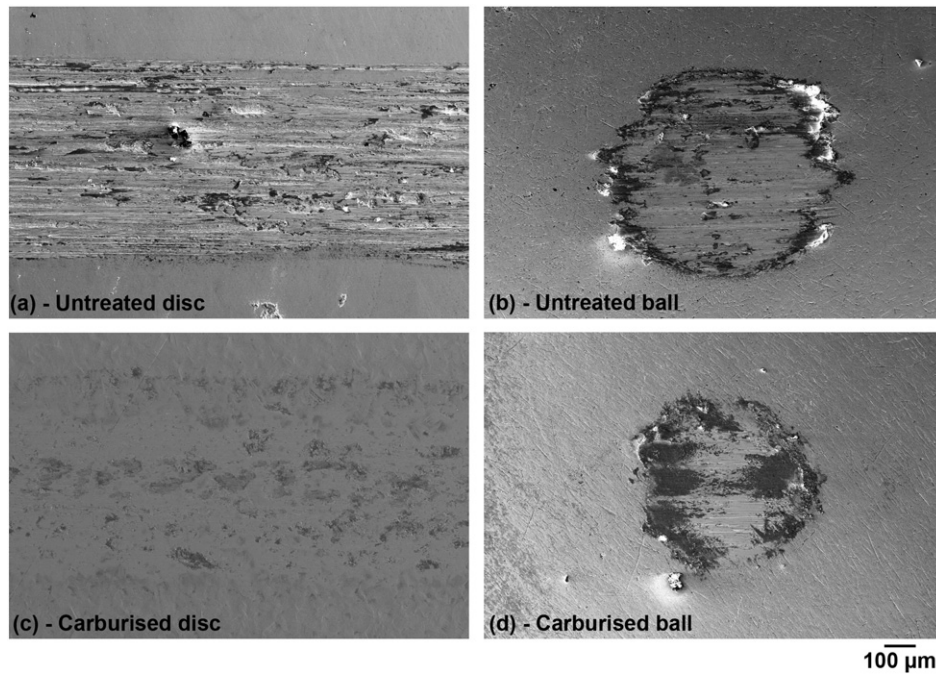


Fig. 5. SEM images post-reciprocating sliding under cathodic potential ( $-700$  mV vs. SCE) of untreated-on-untreated (a) 316LVM disc and (b) 316L ball wear scars and carburised-on-carburised (c) 316LVM disc and (d) 316L ball wear scars.

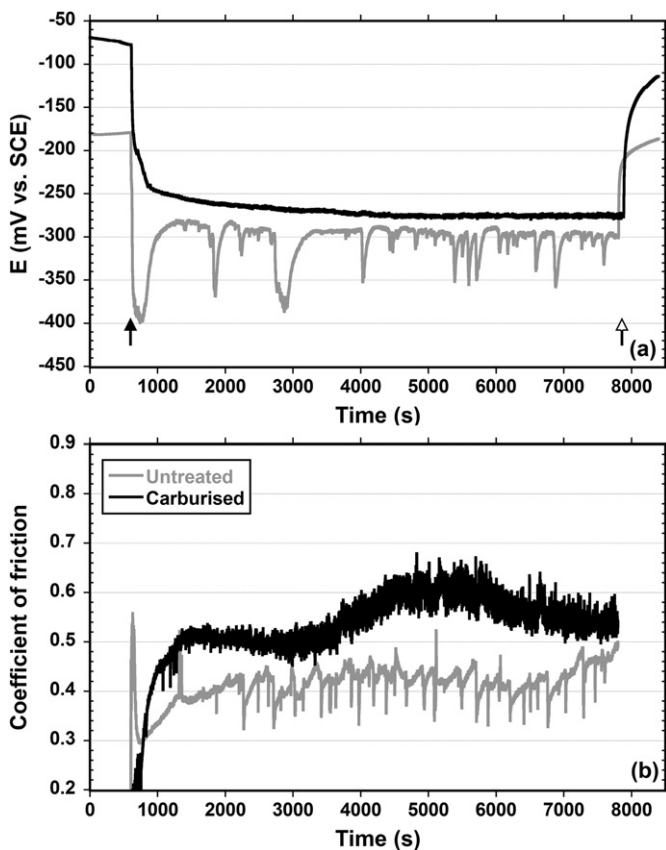


Fig. 6. Open circuit potential plots for untreated-on-untreated and carburised-on-carburised stainless steel tribopairs during reciprocating sliding in Ringer's solution of (a) voltage and (b) coefficient of friction, as a function of time. Black arrow indicates onset of sliding and white arrow indicates termination of sliding.

metal's passive film, if both layers have similar dielectric constants. Therefore, the surface treatment may have increased the kinetics of passive film formation of the 316LVM austenitic stainless steel at the equilibrium potential. Another possibility could be that the untreated metal's passive film has a higher dielectric constants compared to the treated metal. The discrepancy can also be a combination of both the thickness and dielectric constant.

The improvement in corrosion resistance of the passive layer after treatment could have resulted because of the layer's reduction in time constant distribution as well as its thickness. According to Sun et al. [13] the passive film forms much faster on the carburised surface and consequently, it tends to be thicker which also contributes towards the reduction of steady-state current density, hence the increase in polarisation resistance. Sun explains that the expansion of the surface lattice, a consequence of carbon supersaturation, enhances diffusion of film forming elements like chromium, so that the passive film forms more quickly thus enhancing the metal's inherent protection against corrosion.

The EDL's resistance also increased after carburising; however, this increase is not as large as that of the passive layer. The increase in resistance for the 316LVM double layer was from  $126.7 \text{ k}\Omega \text{ cm}^2$  to  $283.3 \text{ k}\Omega \text{ cm}^2$  after surface treatment. The resulting EDL capacitance varied after treatment of the 316LVM austenitic stainless steel. The value of  $Q_1$  was converted to capacitance through Eqs. (6) and (7), which also includes the contribution of the solution resistance [24–27]:

$$\frac{1}{R} = \frac{1}{R_S} + \frac{1}{R_1} \quad (6)$$

$$C_1 = Q_1^{\frac{1}{\alpha_1}} \left( \frac{R_S R_1}{R_S + R_1} \right)^{\frac{1-\alpha_1}{\alpha_1}} \quad (7)$$

The double layer capacitance of the untreated interface is  $26.57 \mu\text{F}/\text{cm}^2$ , while that of the carburised interface is  $10.94 \mu\text{F}/\text{cm}^2$ . The layer capacitance decreased after carburising, which may reflect

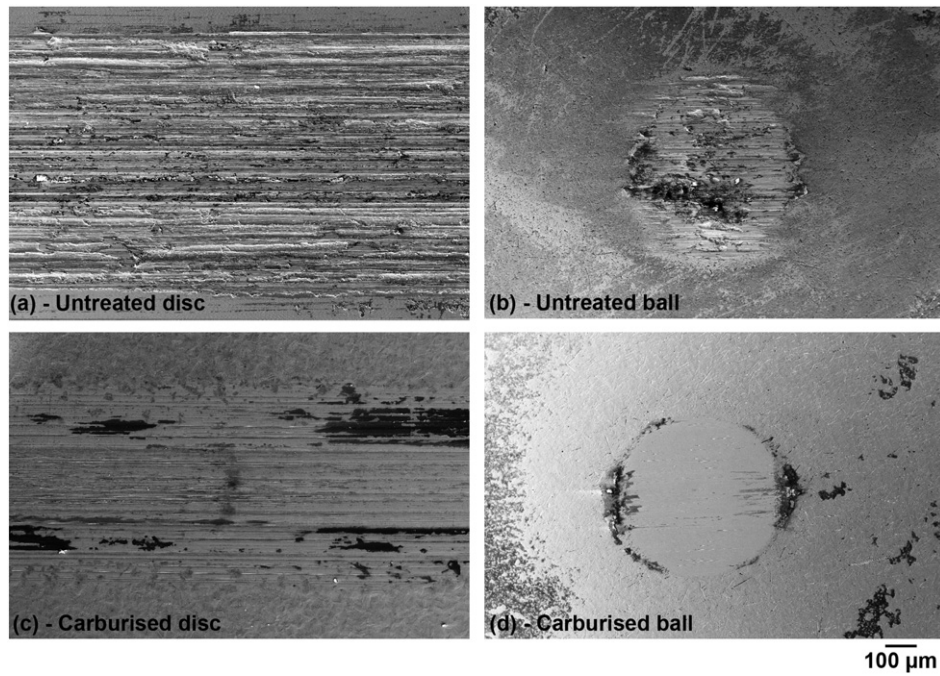


Fig. 7. SEM images post-reciprocating sliding under open circuit potential of untreated-on-untreated (a) 316LVM disc and (b) 316L ball wear scars and carburised-on-carburised (c) 316LVM disc and (d) 316L ball wear scars.

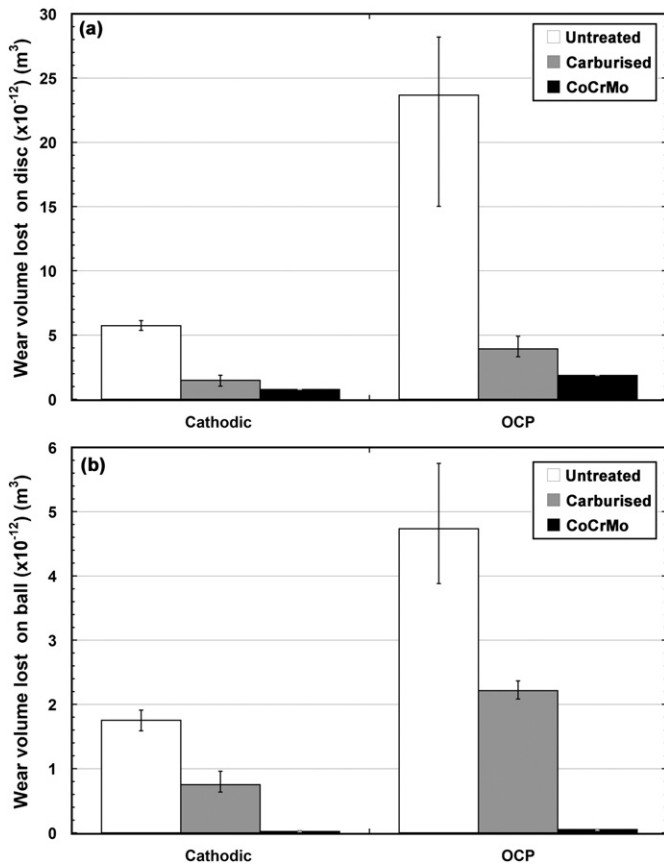
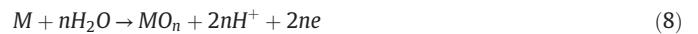


Fig. 8. Volume lost on (a) 316LVM and ASTM F1537 CoCrMo disc and (b) 316L and Stellite® 21 CoCrMo ball after reciprocating sliding in Ringer's solution under cathodic potential ( $-700$  mV) and open circuit potential. CoCrMo-on-CoCrMo is the control sample and error bars reflect the range of values for  $n = 3$ .

thickening of the layer or else reduction in the layer's dielectric constant. The value of  $\alpha_1$  increased, this implying a more stable and homogeneous layer, having less discrepancies in capacitance distribution (hence variation in voltage and current) along the interface.

#### 4.3. Corrosion-wear

The application of a cathodic potential (Fig. 4) prevents metal oxidation. This results in the anodic reaction shown in Eq. (8) being suppressed while the reduction reaction in Eq. (9) being promoted.



At  $-700$  mV versus SCE, the cathodic potential imposed in this study was low enough to suppress oxidation but not excessively low to cause hydrogen evolution, which could have changed the mechanical nature of the surface [33]. The cathodic potential was applied in order to prevent corrosion and thus all recorded material loss was attributed to mechanical wear ( $W_o$ ) and is plotted in Fig. 9. By considering the hardness (Fig. 1 and Table 3) of the surface during cathodic testing, an improvement in volumetric loss was expected for the harder carburised combinations. The higher hardness of the carburised tribopair prevented localised plastic deformation and material detachment. This resulted in a milder form of damage compared to that of the untreated tribopair (Fig. 5) which amounted to a 70% reduction in material loss.

In the OCP test (Fig. 6), the spontaneous OCP drop on the onset of sliding can be principally attributed to the damage and removal of the passive film. In fact when the sliding was halted; the damaged passive film was regenerated as evidenced with the OCP recovery to similar values prior to sliding. There was no evidence of localised corrosion attack in the form of pitting or crevice within the tribopair contact area.

In order to understand the nature of the volumetric loss during metal-on-metal tribocorrosion testing, the synergistic approach was

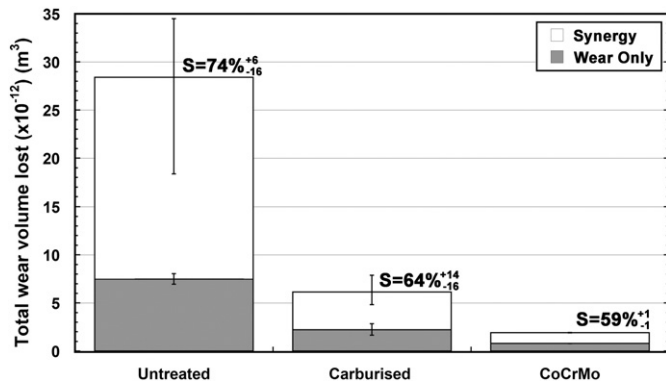


**Fig. 9.** Material lost due to mechanical wear only and synergy on untreated-on-untreated stainless steel, carburised-on-carburised stainless steel and CoCrMo-on-CoCrMo (Control) tribopairs after reciprocating sliding in Ringer's solution under open circuit potential. Error bars reflect the range for wear only ( $W_o$ ) and synergy ( $S$ ) for  $n = 3$ .

used (Fig. 9). The synergistic component for the untreated 316, carburised 316 and CoCrMo tribopairs were 74% (+6% / -16%), 64% (+14% / -16%) and 59% ( $\pm 1\%$ ) respectively. The importance of evaluating the combined effect of corrosion and wear by tribocorrosion testing is highlighted by such results, where the individual wear ( $W_o$ ) and corrosion ( $C_o \approx 0$ ) components are minimal when compared to the synergistic component. Besides exposing metal to corrosion, the effect of removing the passive film for the untreated 316 tribopair implies removing a barrier between two mating surfaces with similar microstructure providing a scenario for adhesion to occur (Fig. 7). Hence the synergy component is due to corrosion due to wear as metal atoms are exposed for oxidation due to passive film damage (Type 1 corrosion-wear [8]).

The OCP trace (Fig. 6) during testing of the untreated tribopair displayed the largest drop on the onset of sliding. This corresponds to an initial running-in period which would have been very effective in disrupting the passive film. The OCP recovered as the friction coefficient reached a steadier state value, highlighting better conformity between the tribopair surfaces. However, the OCP trace was characterised by the repeated fluctuations to lower OCP values during sliding. The corresponding instability in the friction trace (Fig. 6 b) indicate that the observed localised plastic deformation of the wear scar and material detachment (Fig. 7) were impacting negatively on the conformity of the sliding surfaces, resulting in more damage to the passive layer until better tribopair conformity is restored. Therefore, the wear mechanism observed on the untreated tribopair was due to the intensification of the damage and regeneration of the passive film. This led to a very high type I corrosion-wear synergy (Fig. 9). Nonetheless the presence of the passive film aided in the attainment of a lower CoF compared to tests under cathodic protection and potentially contributed to a lower mechanical wear.

For the carburised tribopair the wear mechanism was milder than that observed on the untreated tribopair (Fig. 7). Here the resultant wear scars were smooth albeit minor abrasion marks in the direction of sliding. This has resulted in a smoother surface causing less damage to the passive film. This manifested itself in a small (compared to untreated tribopair) yet very significant material loss via type I corrosion-wear (Fig. 9).

Repeated localised plastic deformation of the surface resulted in work hardening of the untreated tribopair disks which was probably the cause of the formation and propagation of subsurface cracks towards the surface, resulting in delamination and material loss. This wear mechanism was impeded in the carburised tribopair by the very nature of the S-phase microstructure which prohibits adhesion due to its higher yield strength, localised plastic yielding and associated work

hardening. This is because the high density of stacking faults and dislocation entanglement defining the S-phase hinders dislocation cross slip [6]. In the case of the positive control (CoCrMo Tribopair) the behaviour is very similar to that of the carburised stainless steel since under same tribological conditions this material also resists localised plastic deformation and material is principally lost by mild abrasion.

## 5. Conclusions

Based on the experimental results, the following conclusions can be drawn:

1. In direct contact cytocompatibility testing, the results obtained from the human foetal osteoblast (hFOB 1.19) cell line tested showed equal cytocompatibility between the untreated 316LVM, carburised 316LVM and the Thermanox™ positive control. This points to the overall cytocompatibility of the carburised alloy.
2. The passive layer's resistance increased considerably after carburising. Faster film growth kinetics on the carburised surface may be the primary contributor towards improved corrosion resistance after surface treatment. In addition, the distribution of capacitance and time constants decreased within the passive film after carburising. This may have also contributed to the improved impedance.
3. The Electrical Double Layer's resistance increased as well after surface treatment, even though this increase was not as large as that of the passive layer. The EDL's thickness may have increased as well (if the dielectric constants of the untreated and treated layers were similar) and experienced a reduction in time constant dispersion after surface treatment.
4. Carburising improves the localised corrosion resistance of the 316LVM austenitic stainless steel when in contact with deaerated Ringer's solution.
5. The combined wear of S-phase-against-S-phase for 316LVM stainless steel is close to that of the cobalt-based alloy tribo pair under reciprocating sliding wear conditions in Ringer's solution at a maximum contact pressure of approximately 700 MPa.
6. In this work it has been evidenced that carburising can be successfully performed on medical grade 316LVM stainless steel to impart a hard S-phase layer into the surface. The significant increase in hardness is directly related to the amount of diffused carbon species and denotes an imperative role during tribocorrosion tests by instigating a change in wear mechanism, in turn decreasing the amount of worn material and consequently diminishing the synergy component. In the case of the untreated tribopair, wear was dominated by a high degree of plastic deformation, while the carburised tribopair was mostly susceptible to mild abrasive wear.

## Acknowledgements

This research was funded by the following scholarship schemes: Strategic Educational Pathways Scholarship (STEPS); MASTER it!; and the Malta Government Scholarship Scheme (MGSS). These scholarships were part financed by the European Union – European Social Fund (ESF) under Operational Programme II – Cohesion Policy 2007–2013, "Empowering People for More Jobs and a Better Quality of Life". Thanks also go to Bodycote Specialist Technologies GmbH, Germany, for performing the low temperature carburising treatments. The authors are grateful for financial support received from Bodycote Specialist Technologies GmbH, the Faculty of Engineering THINK 10K grant and the University of Malta Research Fund. The authors would also like to thank ERDF (Malta) for financing the testing equipment through the projects: "Developing an Interdisciplinary Material Testing and Rapid Prototyping R&D Facility (Ref. no. 012)" and "Enhancing Health Biotechnology Facilities at the University of Malta (Ref. No. 081)".

## References

- [1] J. Buhagiar, A. Spiteri, M. Sacco, E. Sinagra, H. Dong, Augmentation of crevice corrosion resistance of medical grade 316LVM stainless steel by plasma carburising, *Corros. Sci.* 59 (2012) 169–178.
- [2] F.J. Martin, E.J. Lemieux, T.M. Newbauer, R.A. Bayles, P.M. Natishan, H. Kahn, G.M. Michal, F. Ernst, A.H. Heuer, Carburization-induced passivity of 316L austenitic stainless steel, *Electrochim. Solid-State Lett.* 10 (2007) C76–C78.
- [3] F.J. Martin, P.M. Natishan, E.J. Lemieux, T.M. Newbauer, R.J. Rayne, R.A. Bayles, H. Kahn, G.M. Michal, F. Ernst, A.H. Heuer, Enhanced corrosion resistance of stainless steel carburised at low temperature, *Metall. Mater. Trans. A* 40 (2009) 1805–1810.
- [4] H. Dong, S-phase surface engineering of Fe–Cr, Co–Cr and Ni–Cr alloys, *Int. Mater. Rev.* 55 (2010) 65–98.
- [5] J. Buhagiar, T. Bell, R. Sammons, H. Dong, Evaluation of the biocompatibility of S-phase layers on medical grade austenitic stainless steels, *J. Mater. Sci. Mater. Med.* 22 (2011) 1269–1278.
- [6] J. Buhagiar, A. Jung, D. Gouriou, B. Mallia, H. Dong, S-phase against S-phase tribopairs for biomedical applications, *Wear* 301 (2013) 280–289.
- [7] A.J. Smith, P. Dieppe, K. Vernon, M. Porter, A.W. Blom, Failure rates of stemmed metal-on-metal hip replacements: analysis of data from the National Joint Registry of England and Wales, *Lancet* 379 (2012) 1199–1204.
- [8] P.A. Dearnley, G. Aldrich-Smith, Corrosion–wear mechanisms of hard coated austenitic 316L stainless steels, *Wear* 256 (2004) 491–499.
- [9] J. Qu, P.J. Blau, B.C. Jolly, Tribological properties of stainless steels treated by colossal carbon supersaturation, *Wear* 263 (2007) 719–726.
- [10] S. Thaiwatthana, X.Y. Li, H. Dong, T. Bell, Corrosion wear behaviour of low temperature plasma alloyed 316 austenitic stainless steel, *Surf. Eng.* 19 (2003) 211–216.
- [11] D. Formosa, R. Hunger, A. Spiteri, H. Dong, E. Sinagra, J. Buhagiar, Corrosion behaviour of carbon S-phase created on Ni-free biomedical stainless steel, *Surf. Coat. Technol.* 206 (2012) 3479–3487.
- [12] M. Caligari Conti, A. Karl, P. Schembri Wismayer, J. Buhagiar, Biocompatibility and characterization of a Kolsterised® medical grade cobalt–chromium–molybdenum alloy, *Biomater* 4 (2014), e27713.
- [13] Y. Sun, Depth-profiling electrochemical measurements of low temperature plasma carburised 316L stainless steel in 1 M H<sub>2</sub>SO<sub>4</sub> solution, *Surf. Coat. Technol.* 204 (2010) 2789–2796.
- [14] S.W. Tait, *An Introduction to Electrochemical Testing for Practicing Engineers and Scientists*, Pair O Docs Publications, USA, 1994.
- [15] A. Igual Muñoz, L. Casabán Julián, Influence of electrochemical potential on the tribocorrosion behaviour of high carbon CoCrMo biomedical alloy in simulated body fluids by electrochemical impedance spectroscopy, *Electrochim. Acta* 55 (2010) 5428–5439.
- [16] L. Casabán Julián, A. Igual Muñoz, Influence of microstructure of HC CoCrMo biomedical alloys on the corrosion and wear behaviour in simulated body fluids, *Tribol. Int.* 44 (2011) 318–329.
- [17] C. Valero Vidal, A. Igual Muñoz, Electrochemical aspects in biomedical alloy characterization: electrochemical impedance spectroscopy, in: A. Laskovski (Ed.), *Biomedical Engineering, Trends in Materials Science*, InTech 2011, pp. 283–306.
- [18] M.E. Orazem, B. Tribollet, *Electrochemical Impedance Spectroscopy*, John Wiley & Sons, Inc., NJ, USA, 2008.
- [19] J.-B. Jorcin, M.E. Orazem, N. Pèbère, B. Tribollet, CPE analysis by local electrochemical impedance spectroscopy, *Electrochim. Acta* 51 (2006) 1473–1479.
- [20] J.P. Diard, B. Le Gorrec, C. Montella, Electrical circuits containing CPEs, *Handbook of Electrochemical Impedance Spectroscopy*, BioLogic Science Instruments 2012, pp. 5–11.
- [21] L. Casabán Julián, A. Igual Muñoz, Influence of microstructure of HC CoCrMo biomedical alloys on the corrosion and wear behaviour in simulated body fluids, *Tribol. Int.* 44 (2011) 318–329.
- [22] J.-B. Jorcin, M.E. Orazem, N. Pèbère, B. Tribollet, CPE analysis by local electrochemical impedance spectroscopy, *Electrochim. Acta* 51 (2006) 1473–1479.
- [23] V.D. Jović, B.M. Jović, The influence of the conditions of the ZrO<sub>2</sub> passive film formation on its properties in 1 M NaOH, *Corros. Sci.* 50 (2008) 3063–3069.
- [24] B. Hirschorn, M.E. Orazem, B. Tribollet, V. Vivier, I. Frateur, M. Musiani, Determination of effective capacitance and film thickness from constant-phase-element parameters, *Electrochim. Acta* 55 (2010) 6218–6227.
- [25] C. Valero Vidal, A. Igual Muñoz, Study of the adsorption process of bovine serum albumin on passivated surfaces of CoCrMo biomedical alloy, *Electrochim. Acta* 55 (2010) 8445–8452.
- [26] M.R. Shoar Abouzari, F. Berkemeier, G. Schmitz, D. Wilmer, On the physical interpretation of constant phase elements, *Solid State Ionics* 180 (2009) 922–927.
- [27] N.P. Cosman, K. Fatih, S.G. Roscoe, Electrochemical impedance spectroscopy study of the adsorption behaviour of  $\alpha$ -lactalbumin and  $\beta$ -casein at stainless steel, *J. Electroanal. Chem.* 574 (2005) 261–271.
- [28] F. Mohammadi, T. Nickchi, M.M. Attar, A. Alfantazi, EIS study of potentiostatically formed passive film on 304 stainless steel, *Electrochim. Acta* 56 (2011) 8727–8733.
- [29] J.J. Gray, C.A. Orme, Electrochemical impedance spectroscopy study of the passive films of alloy 22 in low pH nitrate and chloride environments, *Electrochim. Acta* 52 (2007) 2370–2375.
- [30] V. Freger, S. Bason, Characterization of ion transport in thin films using electrochemical impedance spectroscopy: I. Principles and theory, *J. Membrane Sci.* 302 (2007) 1–9.
- [31] A. Kocijan, D.K. Merl, M. Jenko, The corrosion behaviour of austenitic and duplex stainless steels in artificial saliva with the addition of fluoride, *Corros. Sci.* 53 (2011) 776–783.
- [32] D. Wallinder, J. Pan, C. Leygraf, A. Delblanc-Bauer, EIS and XPS study of surface modification of 316LVM stainless steel after passivation, *Corros. Sci.* 41 (1998) 275–289.
- [33] Y. Yan, A. Neville, D. Dowson, Tribo-corrosion properties of cobalt-based medical implant alloys in simulated biological environments, *Wear* 263 (2007) 1105–1111.